ADVANCES IN ATMOSPHERIC SCIENCES, VOL. 37, NOVEMBER 2020, 1222–1238

• **Original Paper** •

Characteristics of Fengyun-4A Satellite Atmospheric Motion Vectors and Their Impacts on Data Assimilation

Yaodeng CHEN*[1], Jie SHEN[1], Shuiyong FAN*[2], Deming MENG[1], and Cheng WANG[1]

[1]*Key Laboratory of Meteorological Disaster of Ministry of Education/Collaborative Innovation Center on Forecast and Evaluation of Meteorological Disasters*, *Nanjing University of Information Science and Technology*, *Nanjing* 210044, *China*

[2]*Institute of Urban Meteorology*, *China Meteorological Administration*, *Beijing* 100089, *China*

(Received 19 April 2020; revised 10 July 2020; accepted 27 July 2020)

ABSTRACT

The high observation efficiency, scanning speed and observation frequency of the Fengyun-4A (FY-4A) satellite indicates the progress of Chinese geostationary meteorological satellites. The characteristics of FY-4A atmospheric motion vectors (AMVs) derived from the high-level water vapor (WV-High) channel, mid-level water vapor (WV-Mid) channel, and infrared (IR) channel of FY-4A are analyzed, and their corresponding observation errors estimated. Then, the impacts of single-channel and multi-channel FY-4A AMVs on RMAPS-ST (the Rapid-refresh Multi-scale Analysis and Prediction System—Short Term) are evaluated based on one-month data assimilation cycling and forecasting experiments. Results show that the observation errors of FY-4A AMVs from the three channels have an explicit vertical structure. Results from the cycling experiments indicate that the assimilation of AMVs from WV-High produces more apparent improvement of the wind in the upper layer, while a more positive effect in the lower layer is achieved by the assimilation of AMVs from IR. Furthermore, the assimilation of AMVs from IR is more skillful for medium and moderate precipitation than from other channels owing to the good quality of data in the lower layer in the AMVs from IR. Assimilation of FY-4A AMVs from the three channels could combine the advantages of assimilation from each individual channel to improve the wind in the upper, middle and lower layers simultaneously.

Key words: data assimilation, FY-4A satellite, atmospheric motion vector, observation error

Citation: Chen, Y. D., J. Shen, S. Y. Fan, D. M. Meng, and C. Wang, 2020: Characteristics of Fengyun-4A satellite atmospheric motion vectors and their impacts on data assimilation. *Adv. Atmos. Sci.*, **37**(11), 1222–1238, https://doi.org/10.1007/s00376-020-0080-0.

Article Highlights:

- New observation errors of FY-4A AMVs show a more obvious vertical structure, which may be more reasonable for the use of AMVs
- FY-4A AMVs from water vapor channels improve wind in the upper layer, while AMVs from the infrared channel improve the lower layer
- Multi-channel assimilation of FY-4A AMVs could combine advantage of assimilation from each channel and improve most layers simultaneously

1. Introduction

Atmospheric motion vectors (AMVs) are wind observations derived from consecutive satellite images by tracking features such as cirrus edges, gradients in water vapor, or small cumulus clusters (Nieman et al., 1993; Velden et al., 1997). They mainly describe the wind field in the middle and upper troposphere, which could effectively make up for the deficiency of the upper observation data. AMVs have been investigated since the 1970s and applied in operational numerical weather prediction (NWP) systems since the 1990s (Schmetz et al., 1993; Menzel, 2001). Various studies have pointed out that the assimilation of AMVs can improve the atmospheric dynamics condition, which in turn increases the accuracy of NWP (Wang et al., 2006; Goerss, 2009; Berger et al., 2011; Joo et al., 2013; Wu et al., 2014).

Compared to other wind measurements, AMVs from geostationary satellites can provide superior temporal and spatial coverage in the middle and upper troposphere (Kaur et

* Corresponding authors: Yaodeng CHEN, Shuiyong FAN
Email: keyu@nuist.edu.cn, syfan@ium.cn

al., 2015), due to the capability of geostationary satellites in achieving frequent and continuous observations over a specific region (Honda et al., 2018). Various studies on the assimilation of AMVs derived from different satellites have been carried out to take advantage of such exceptional temporal and spatial overage, and positive results obtained. For example, AMVs from the Geostationary Operational Environment Satellite (GOES) have been assimilated in hurricane research, and the forecasts of hurricane tracks and intensity improved (Soden et al., 2001; Velden et al., 2017; Li et al., 2020). The assimilation of Kalpana-1 AMVs also reduced the initial position errors and improved track forecasts of tropical cyclones (Deb et al., 2011). Besides, studies on the assimilation of AMVs from MTSAT (Multi-function Transmission Satellite) and Himawari-8 showed positive impacts on the timing and intensity of rainfall forecasts, and even flood risk prediction (Yamashita, 2012; Otsuka et al., 2015; Kunii et al., 2016).

In addition to the satellites mentioned above, Fengyun (FY) geostationary satellites from China have also provided AMV products for operational NWP systems and the research community. Since the launch of the first Chinese geostationary meteorological satellite, FY-2A, in 1997, studies and applications of AMVs from Chinese geostationary meteorological satellites have been gradually increasing (Feng et al., 2008; Ren et al., 2014; Wan et al., 2018). Compared to the FY-2 series, the spatial and temporal resolutions have been dramatically improved in the FY-4A satellite, and two visible channels and seven infrared (IR) channels included. Moreover, it can produce full-disk imagery every 15 minutes, and the temporal resolution can be increased to up to 5 minutes for the coverage of China (Dong, 2016; Zhang et al., 2017; Wang and Shen, 2018; Zhao et al., 2019). The capability of obtaining AMVs has been greatly increased. However, studies on the AMV products of FY-4A are relatively rare (Wan et al., 2019). Therefore, in order to further understand the characteristics of FY-4A AMVs, and to promote the application of FY-4A AMVs in NWP, the characteristics of AMV products are analyzed in this study, and their impacts on data assimilation discussed.

The rest of this paper is organized as follows: Section 2 analyzes the characteristics of FY-4A AMVs, and the observation error of AMV products is estimated in section 3. Section 4 describes the framework of the assimilation and forecasting experiments, and results are discussed in section 5. Section 6 provides a summary of the study's key findings.

2. FY-4A AMVs and their characteristics

2.1. *AMV data from FY-4A*

The monitoring and prediction of severe weather systems is one of the most important and complicated parts of operational weather forecasting. The Advanced Geosynchronous Radiation Imager (AGRI) onboard the FY-4A geostationary meteorological satellite plays a critical role in the monitoring of severe weather systems in China and its surrounding areas. There are 14 channels in AGRI, and AMV products used in this study are derived from channel 09 (λ = 6.5 μm), channel 10 (λ = 7.2 μm) and channel 12 (λ = 11.0 μm); namely, the high-level water vapor (WV-High) channel, the mid-level water vapor (WV-Mid) channel, and the IR channel, respectively. According to the documentation for FY-4A AMV products, the spatial resolution corresponding to the sub-satellite point is 64 km, and products with 3-h resolution can be provided. The horizontal distribution of FY-4A AMVs from WV-High, WV-Mid and IR at 0000 UTC 1 November 2018 are displayed in Figs. 1a–c. It is shown that the AMVs cover the West Pacific and Indian oceans, where conventional observations are sparse. Meanwhile, the horizontal distribution of AMVs from WV-High and WV-Mid are similar but different from that of IR. The IR channel supplements the AMV data of some regions where two water vapor channels are not observed. Figure 1d shows the calculation of the vertical profile of the total number of FY-4A AMVs for the three channels from 1–30 November 2018. The vertical distribution of AMVs derived from the two water vapor channels is obviously different from that from the IR channel, which is due to the difference in absorption characteristics of each channel. More specifically, WV-High and WV-Mid are in the water vapor absorption bands (Velden et al., 1997), and their different weighting function peak heights lead to the discrepancy in heights at which the channel AMV count is the most. In contrast, the IR channel is in the IR window band (Yang et al., 2014, Lu et al., 2017), so it can obtain AMVs of various heights, even data on the middle and lower troposphere.

2.2. *Quality indicator for AMVs*

The quality indicator (QI) is a weighted average of several normalized QI components, which is calculated to represent the quality of each FY-4A AMV (Holmlund, 1998). The QI value of FY-4A AMV is provided by the National Satellite Meteorological Center of China of the China Meteorological Administration (CMA). It is calculated as an empirical function of a spatial and temporal consistency check of wind speed, wind direction, vector and horizontal wind components. The value decreases as the agreement of a given vector with its surroundings decreases. As a result, a larger QI value means a higher credibility (Velden et al., 1998; Deb et al., 2015).

Figure 2 shows the vertical distributions of FY-4A AMVs derived from the three channels from 1–30 November 2018 with different QI values. It can be seen that AMVs with different QI thresholds have similar vertical structure but the proportion of total amount is different. For example, AMVs with QI greater than 70 account for more than 80%, AMVs with QI greater than 80 make up about 60%, and AMVs with QI greater than 90 share only approximately 30% of the total data quantity.

Next, the wind speed bias (Fig. 3) and root-mean-square error (RMSE) (Fig. 4) of FY-4A AMVs in November 2018 are calculated against the Final Operational Global Analysis (FNL) for FY-4A AMVs with different QI

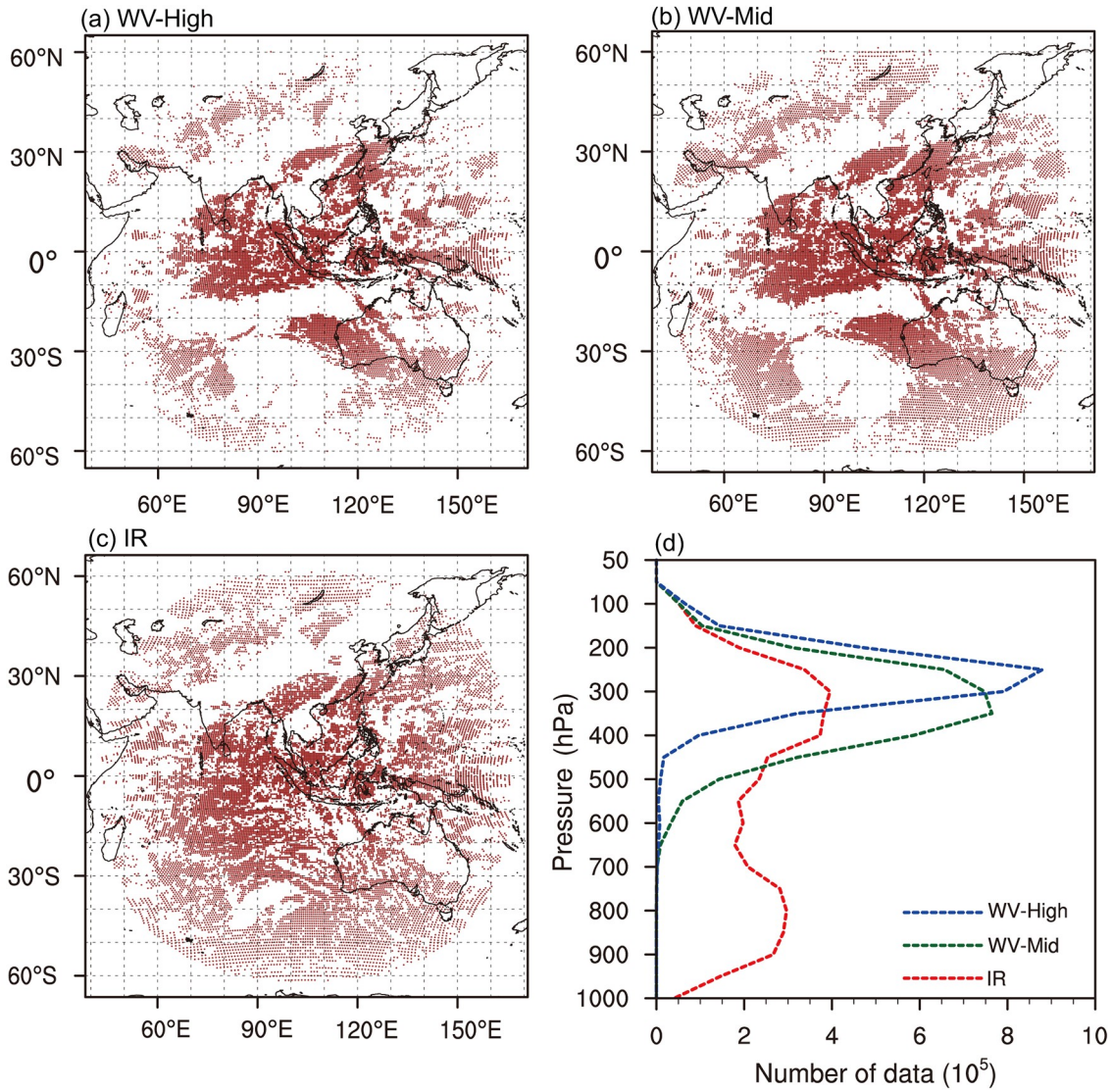

Fig. 1. Horizontal distributions of AMVs derived from (a) WV-High, (b) WV-Mid, and (c) IR at 0000 UTC 1 November 2018, and (d) vertical profiles of the total number of single AMV data from the three channels in each layer for the period from 1–30 November 2018.

thresholds. As displayed in Fig. 3 and Fig. 4, smaller speed bias and RMSE of AMVs are obtained with a larger QI value, which is consistent with the conclusion obtained by Kim and Kim (2018). However, as the primary source of FY-4A AMVs below 500 hPa, data from the IR channel with QI greater than 80 (red line in Fig. 3c) have a slightly smaller wind speed bias than that with other thresholds, which is related to the AMV products themselves.

Besides, the probability density function (PDF) of deviation for AMV data with the three QI values against FNL is shown in Fig. 5. In order to analyze FY-4A AMVs conveniently, AMV data are divided into three bins according to height; namely, the upper layer (400–50 hPa), middle layer (700–400 hPa) and lower layer (1000–700 hPa). It can be seen that fewer outliers with negative deviation are found in a larger QI threshold, making the deviation distribution more symmetric. At the same time, FY-4A AMVs from the two water vapor channels have a poor PDF distribution in the lower layer owing to its small number of samples.

Taking the data amount and quality (bias, RMSE and PDF) of the three channels into consideration, AMVs with QI greater than 80 will be extracted from products for subsequent research, and AMVs below 700 hPa in the two water vapor channels will not be assimilated.

3. Observation error estimation

Both observation error and background error determine the effect of the observation on the background in the assimilation. It is of great importance to estimate the reasonable observation error before assimilating a new kind of observation (Errico et al., 2001). Otsuka et al. (2018) analyzed the error characteristics of Rapid Scan AMVs from Himawari-8, and found that AMVs derived from different

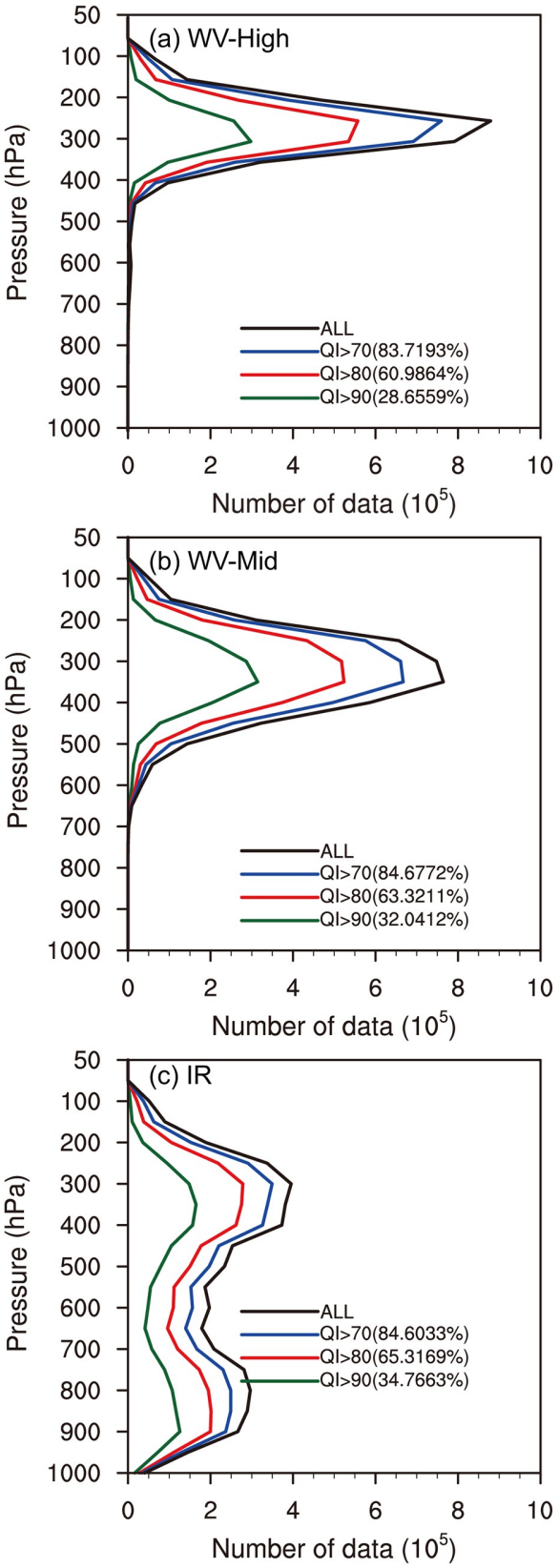

Fig. 2. Vertical distributions of AMVs derived from (a) WV-High, (b) WV-Mid, and (c) IR for the period from 1–30 November 2018 with different QI values (the values in brackets represent the percentage of the total amount of data under this threshold).

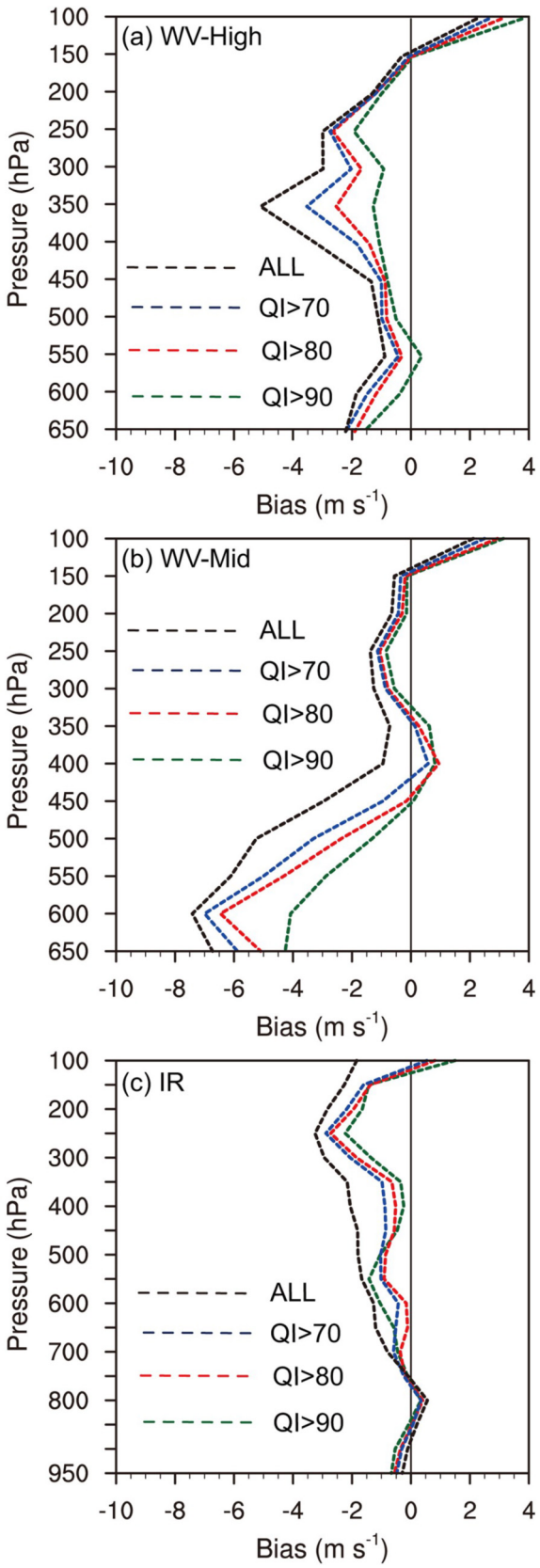

Fig. 3. Average wind speed bias against FNL AMVs derived from (a) WV-High, (b) WV-Mid, and (c) IR in November 2018 (the black solid line denotes that the bias of AMV data is zero).

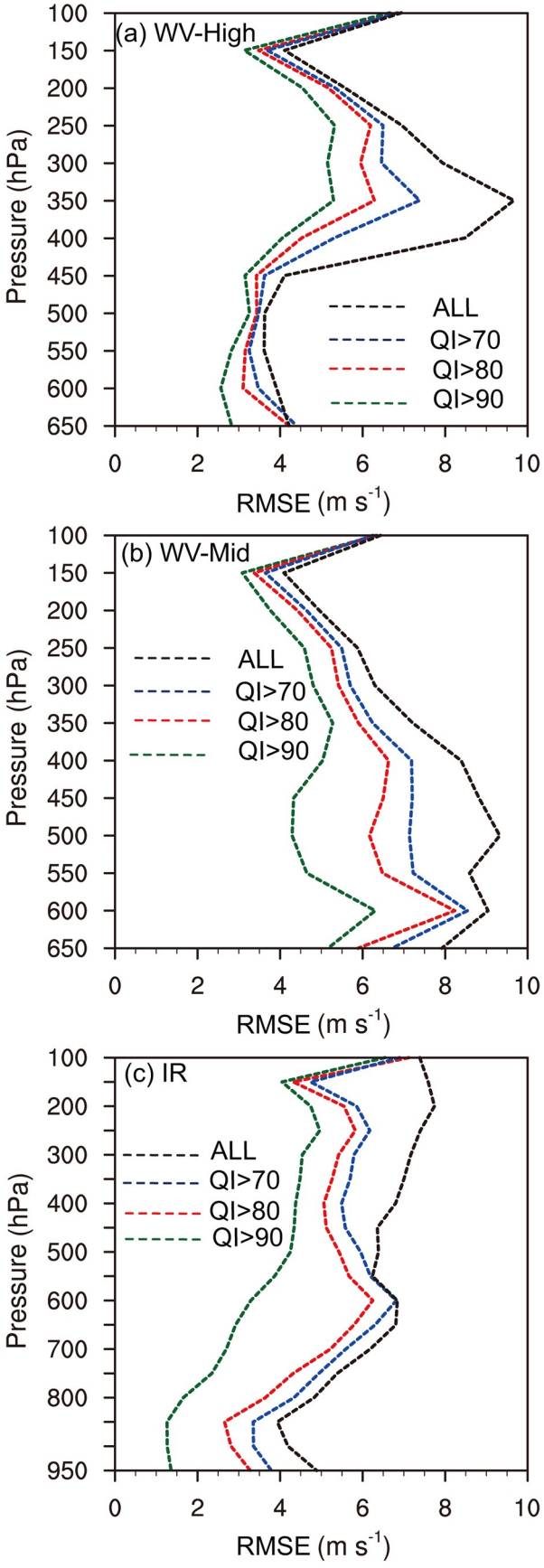

Fig. 4. Average wind speed RMSE against FNL AMVs derived from (a) WV-High, (b) WV-Mid, and (c) IR in November 2018.

channels have different characteristics, suggesting the need to calculate the observation error of each channel.

Conventional observation data or reanalysis data are often used as reference fields in the observation error statistics. The RMSE is usually regarded as the observation error on the premise that the observation is not related to the reference field (Benjamin et al., 1998; Gao et al., 2012). Most previous studies estimated AMV observation error through direct comparison between AMVs with radiosonde data (Hollingsworth and Lönnberg, 1986; Bormann et al., 2003; Bedka et al., 2008). As radiosonde data are too sparse in terms of spatial and temporal resolution compared to FY-4A AMVs, if selected as reference fields, fewer samples of data pairs could be selected and therefore representative errors would be caused. Therefore, the FNL reanalysis is used as the reference field in this study.

Referring to the layered criterion in the default observation error file from the Weather Research and Forecasting Model Data Assimilation (WRFDA) system and the statistical method used in Cordoba et al. (2017) and Desroziers et al. (2005), the model layer is vertically divided into n layers at an interval of 50 hPa. The number of AMV data at each layer is recorded as $m_j\,(j=1,2,3,\cdots,n)$. An assumption is made that the error statistics at each layer are homogeneous. Hence, the corresponding observation error at the jth layer $(j=1,2,3,\cdots,n)$ is recorded as

$$\boldsymbol{R}_{\text{new}}(j)=\left\{\frac{1}{m_j}\sum_{i=1}^{i=m_j}\left[\boldsymbol{y}-H(\boldsymbol{x}_{\text{b},i})\right]\left[\boldsymbol{y}-H(\boldsymbol{x}_{\text{b},i})\right]\right\}^{\frac{1}{2}},\quad (j=1,2,3,\cdots,n),$$

where $\boldsymbol{y}$, $\boldsymbol{x}_{\text{b}}$ and H denote the FY-4A AMV observations, reference background fields, and nonlinear observation operator, respectively. It should be noted that the observation passing quality control is used here for error statistics.

Figure 6 shows the AMV observation error profiles for the three channels averaged from 1–30 November 2018. Compared to default observation errors, the new observation errors vary with height obviously. The error profiles of the three channels have similar structure and comparable values above 400 hPa. However, between 700 hPa and 400 hPa, the observation errors of WV-High (R_{wvh}) increase with height, while the observation errors of WV-Mid (R_{wvm}) and IR (R_{ir}) decrease with height.

In terms of the specific values, R_{wvh} is greater than the default error above 400 hPa, but less than the default error below 400 hPa. R_{wvm} is greater than the default error in the upper and middle layers, which will weaken the weight of observation. As for R_{ir}, it has smaller values below 800 hPa and larger values above 800 hPa. In addition, it is shown that the minimum values of the new observation errors exist at 200 hPa in R_{wvh}, R_{wvm} and R_{ir}, and all of them are smaller than the default error in WRFDA (4.5 m s^{-1}).

A more accurate observation error value is conducive to a more reasonable estimation of the weight of AMV observations in the process of assimilation, leading to a better 3D

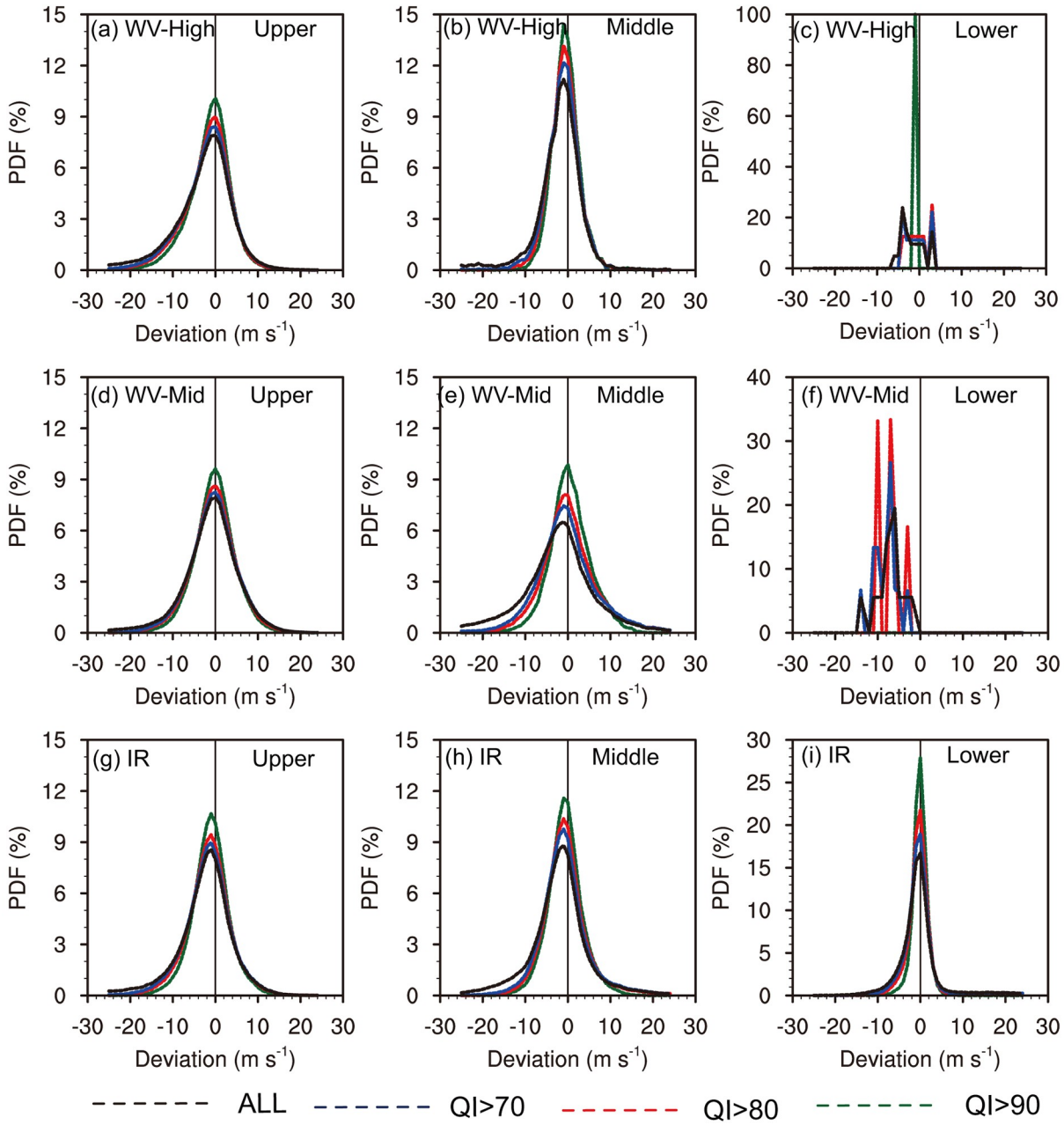

Fig. 5. PDF of deviation of AMVs derived from (a–c) WV-High, (d–f) WV-Mid and (g–i) IR in the upper layer (above 400 hPa), middle layer (400–700 hPa) and lower layer (below 700 hPa).

wind field analysis. Thus, new observation errors of the three channels will be applied to the subsequent assimilation experiments.

4. Experimental framework

4.1. *Model configuration*

This study is based on the Rapid-refresh Multi-scale Analysis and Prediction System—Short Term (RMAPS-ST), which runs operationally at the Beijing Meteorological Bureau (Fan et al., 2013; Chen et al., 2014; He et al., 2019; Xie et al., 2019). In RMAPS-ST, the Advanced Research version of the WRF model, version 3.9, and the WRFDA system are employed. Assimilation is performed on a large domain with a grid spacing of 9 km and 649 × 500 grid points, using 51 vertical levels laid out with an upper limit of 50 hPa.

The experimental domain is shown in Fig. 7 with the distribution of the main conventional observations at 0000 UTC 1 November 2018. AMVs derived from the WV-High, WV-Mid and IR channels are assimilated in this study by merging with conventional observations. Both the initial and boundary conditions are obtained from the Global Forecast

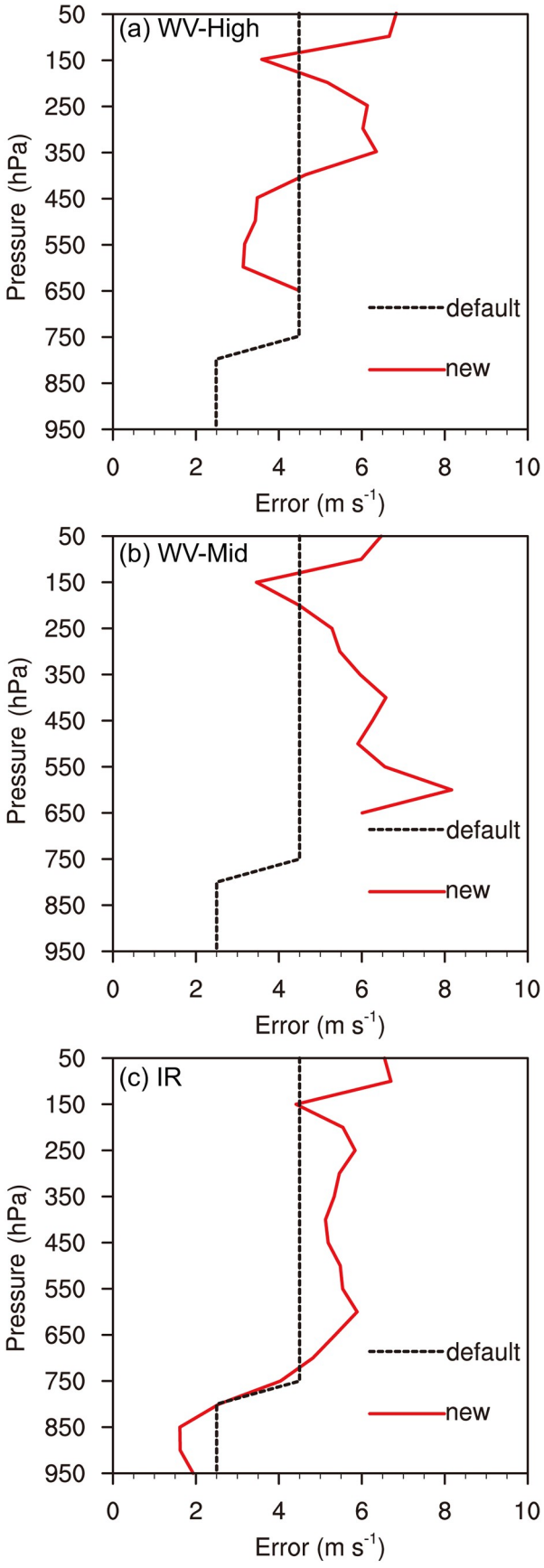

Fig. 6. Vertical profiles of default observation error (black dotted line) and new observation error (red line) of AMVs for (a) WV-High, (b) WV-Mid and (c) IR (units: m s^{-1}).

System produced by the National Centers for Environmental Prediction. The Thompson microphysics scheme (Thompson et al., 2008) and RRTMG long- and shortwave radiation scheme (Iacono et al., 2008) are used. In addition, the Kain–Fritsch cumulus parameterization scheme (Kain, 2004) is also adopted in this domain.

4.2. *Experimental setup*

Capability to assimilate AMVs derived from the three channels with new observation errors has been implemented within RMAPS-ST in this study. Five experiments (Table 1) are configured to investigate the added value from the assimilation of FY-4A AMVs on analyses and forecasts with new observation error. Firstly, the control experiment only assimilates the conventional observations (hereafter CTRL). Then, AMVs from WV-High (CONWVh), WV-Mid (CONWVm) and IR (CONIR) are assimilated together with conventional data, respectively. Moreover, an experiment with AMVs from the three channels assimilated simultaneously (CONALL) is added as well. Additionally, to better display the impact of the new observation error on analyses and forecasts, an experiment assimilating three-channel AMVs with default observation error in WRFDA is necessary, and is named CONALL-DEF.

In the six experiments, partial cycle operation (Hsiao et al., 2012) is adopted at 0000 UTC every day, which means that the initial field of 0000 UTC comes from a 6-h forecast beginning at 1800 UTC of the previous day. Then, the assimilation runs eight times at 0000, 0300, 0600, 0900, 1200, 1500, 1800 and 2100 UTC per day with 3-h cycling. At each analysis time, data within a 3-h window centered on the synoptic time will be ingested and a 24-h forecast will be obtained.

5. Results and discussion

5.1. *Data absorption ratio*

Table 2 calculates the average proportion of the AMVs absorbed by the assimilation system to the total AMVs used in each assimilation process from experiments with new observation errors first. On average, more than 90% of the data are absorbed in each assimilation cycle, indicating the utilization rate of FY-4A AMVs from the three channels with QI greater than 80 is relatively high. Since observations from radiosondes are obtained twice a day at 0000 UTC and 1200 UTC, the time series of AMV observation minus background (OMB) and AMV observation minus analysis (OMA) of horizontal wind components at 1200 UTC are statistically analyzed in Fig. 8. It can be seen from the time series of OMB (Figs. 8a and c), the U component in FY-4A AMVs is smaller than the background, while the V component is larger than the background. However, the assimilation clearly reduces the deviation between the analysis and observation (Figs. 8b and d), with a more stable time series and a weakened amplitude.

Moreover, the OMB sequence obtained by simultaneous assimilation of AMVs from the three channels is stable

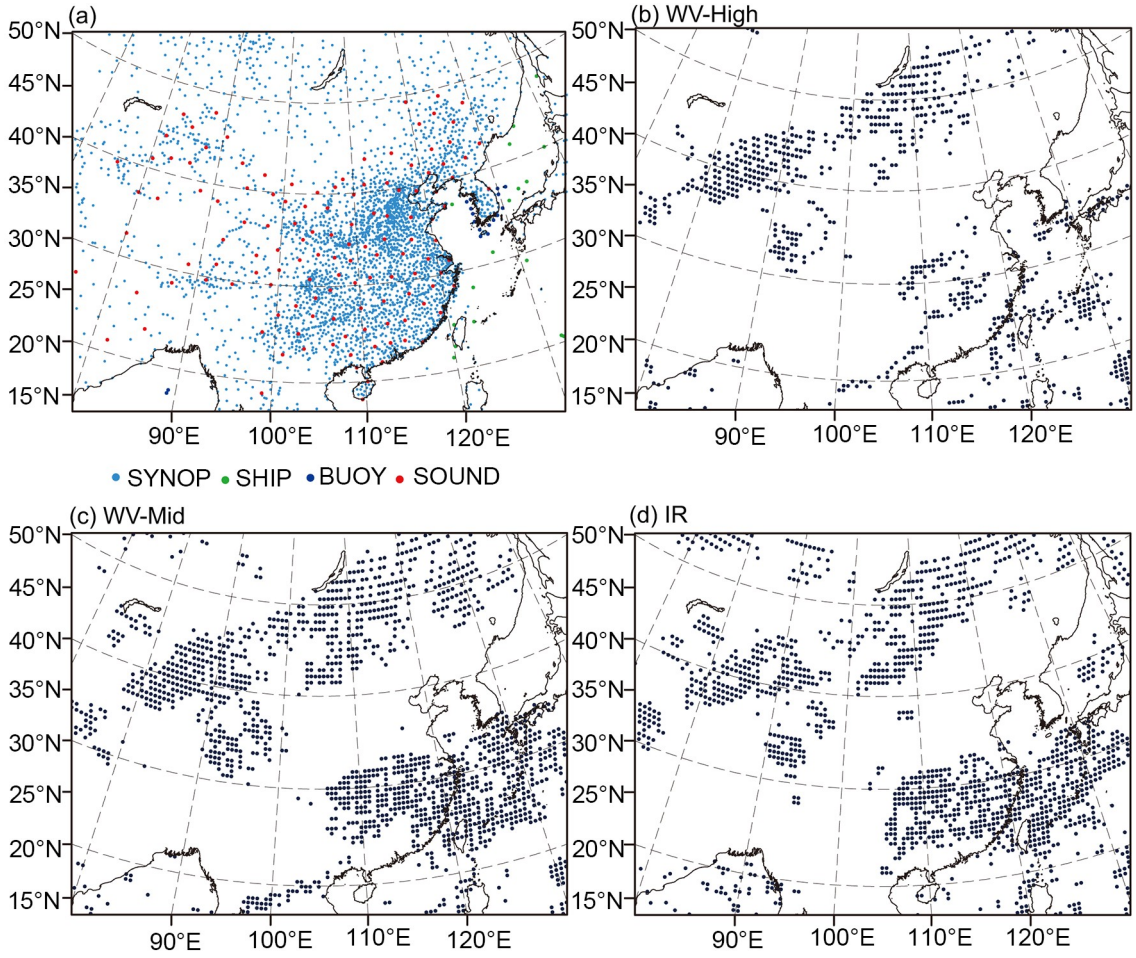

Fig. 7. Domain of the model and the locations of the (a) main types of conventional observation data, (b) WV-High AMVs, (c) WV-Mid AMVs and (d) IR AMVs (SYNOP denotes surface station observations; SHIP denotes ship observations; BUOY denotes buoy observations, and SOUND denotes radiosonde observations).

Table 1. Experiment design schemes.

Experiment	Observation error	Assimilation data
CTRL	Default value defined in WRFDA	Conventional observations
CONWVh	New observation error R_{wvh}	AMVs from WV-High Conventional observations
CONWVm	New observation error R_{wvm}	AMVs from WV-Mid Conventional observations
CONIR	New observation error R_{ir}	AMVs from IR Conventional observations
CONALL	New observation error R_{wvh}, R_{wvm} and R_{ir} for each channel	Conventional observations AMVs from three channels
CONALL-DEF	Default observation error in WRFDA	Conventional observations AMVs from three channels

Table 2. Average absorption ratios (%) of AMVs in different layers (hPa) from experiments assimilating with new observation errors.

	Layers (hPa)								
Experiment	900–1000	800–900	800–700	700–600	600–400	400–300	300–200	200–100	100–50
CONWVh	–	–	–	99.6	99.97	99.94	99.95	99.99	99.99
CONWVm	–	–	–	99.99	99.98	99.96	99.97	99.99	99.99
CONIR	97.5	98.7	99.84	99.96	99.9	99.98	99.98	99.99	99.99
CONALL	97.5	98.7	99.79	99.89	99.93	99.96	99.96	99.97	99.99

with no obvious outliers under the mutual restriction of data from the three channels. Also, the OMA is closer to 0 than that of the single-channel assimilation experiments, which means that the wind analysis obtained from the multi-channel assimilation experiment is better than that from the single-channel assimilation experiments.

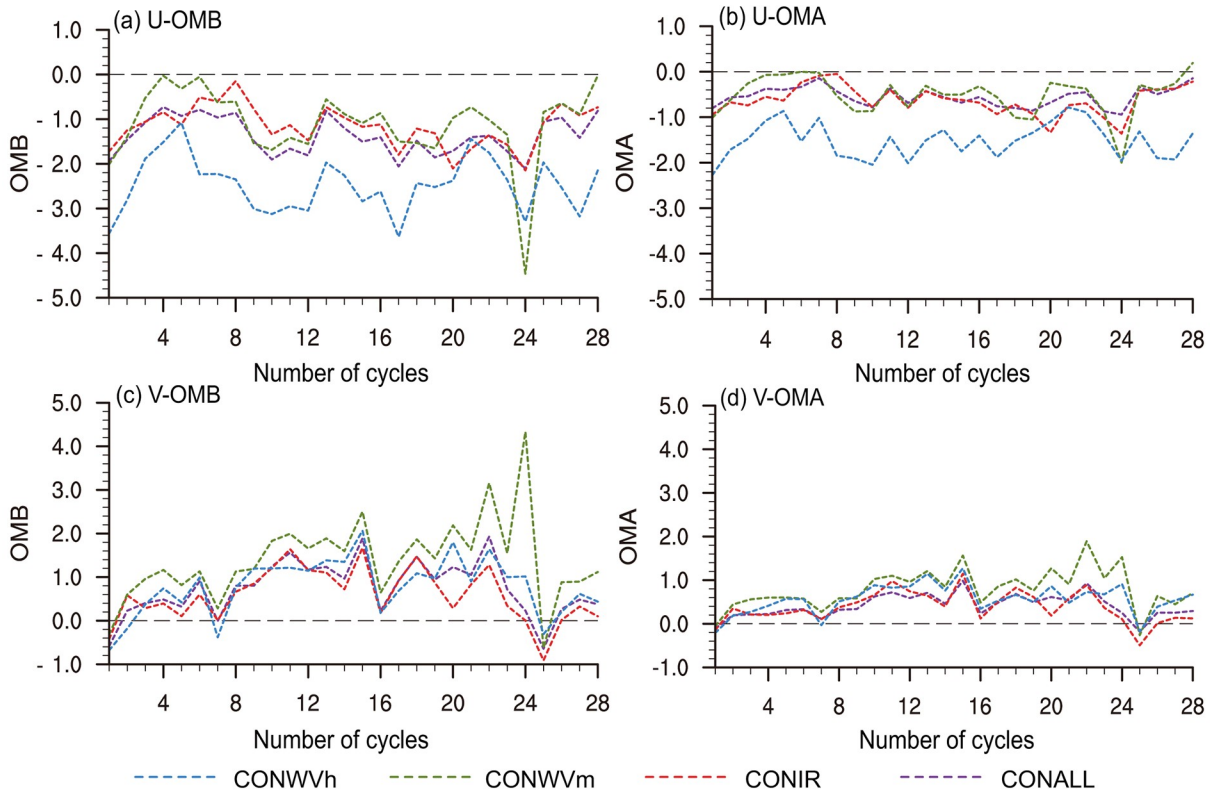

Fig. 8. Time series of the (a, c) OMB and (b, d) OMA statistics of the *U* and *V* components for assimilating FY-4A AMVs at 1200 UTC from the experiment assimilating FY-4A AMVs with new observation errors.

5.2. *Verification for single-channel assimilation*

The RMSEs for the analysis and forecast against sounding observations are calculated by the Model Evaluation Tools (MET) verification package (Kirby, 2004), which is designed to be a highly configurable, state-of-the-art suite of verification tools. MET provides a variety of verification techniques, including standard verification scores comparing gridded model data obtained from the WRF modeling system with point-based observations.

5.2.1. *Wind fields*

Since the AMV products mainly contain wind field information, only horizontal wind components (*U* and *V*) are discussed. Figure 9 shows the vertical profiles of the mean analysis RMSEs for horizontal winds (*U*, *V*) (solid lines) and the forecast RMSEs at *t*+6 h (dashed lines) and *t*+24 h (dotted lines) of CTRL and the experiments assimilating the single-channel AMVs. The experiments assimilating FY-4A AMVs achieve comparable analysis with CTRL, and even slightly inferior to CTRL, especially for the *U* component at 300 hPa, which may be related to the sparse resolution of the reference radiosonde observations.

After 6-h forecasts, the experiments assimilating FY-4A AMVs reduce the RMSEs in wind fields compared to CTRL. Positive effects mainly occur in the upper and middle layers, which is in accordance with the layer where FY-4A AMVs are distributed (Fig. 1d). Besides, among the three channels, the assimilation of WV-High AMVs produces more obvious improvement, while AMVs from the other two channels have a relatively weak effect on the 6-h forecast. After 24-h forecasts, the RMSEs of the horizontal wind components become larger, and the advantage of assimilating FY-4A AMVs gradually diminishes, but still appears in the *U* component below 500 hPa and *V* component above 500 hPa. Moreover, AMVs from the IR channel have a clearer positive impact on the 24-h forecast than that from the two water vapor channels.

At the same time, the mean RMSEs in the three layers for different experiments are calculated for various lead times. The results (Fig. 10) show that the assimilation of FY-4A AMVs reduces the RMSEs of the *U* and *V* components in the upper layer, and the improvement can even be seen in the 24-h forecast. Focusing in the middle and lower layers, AMVs from the two water vapor channels produce little positive effect because of no observations below 700 hPa. However, the assimilation of AMVs from IR improves the forecast of the *V* component in the middle layer, and improvement of the horizontal components in the lower layers in CONIR is gradually shown after 18 h of forecasting.

In terms of the vertical distribution of FY-4A AMVs, a large number of AMVs from the three channels concentrate at 300 hPa, while only AMVs from IR are available below 700 hPa. Figure 11 displays the trend of RMSEs at 300 hPa and 700 hPa with lead time. It is clear that AMVs derived from the two water vapor channels have an advantage in improving the forecast in the upper layer, especially the data

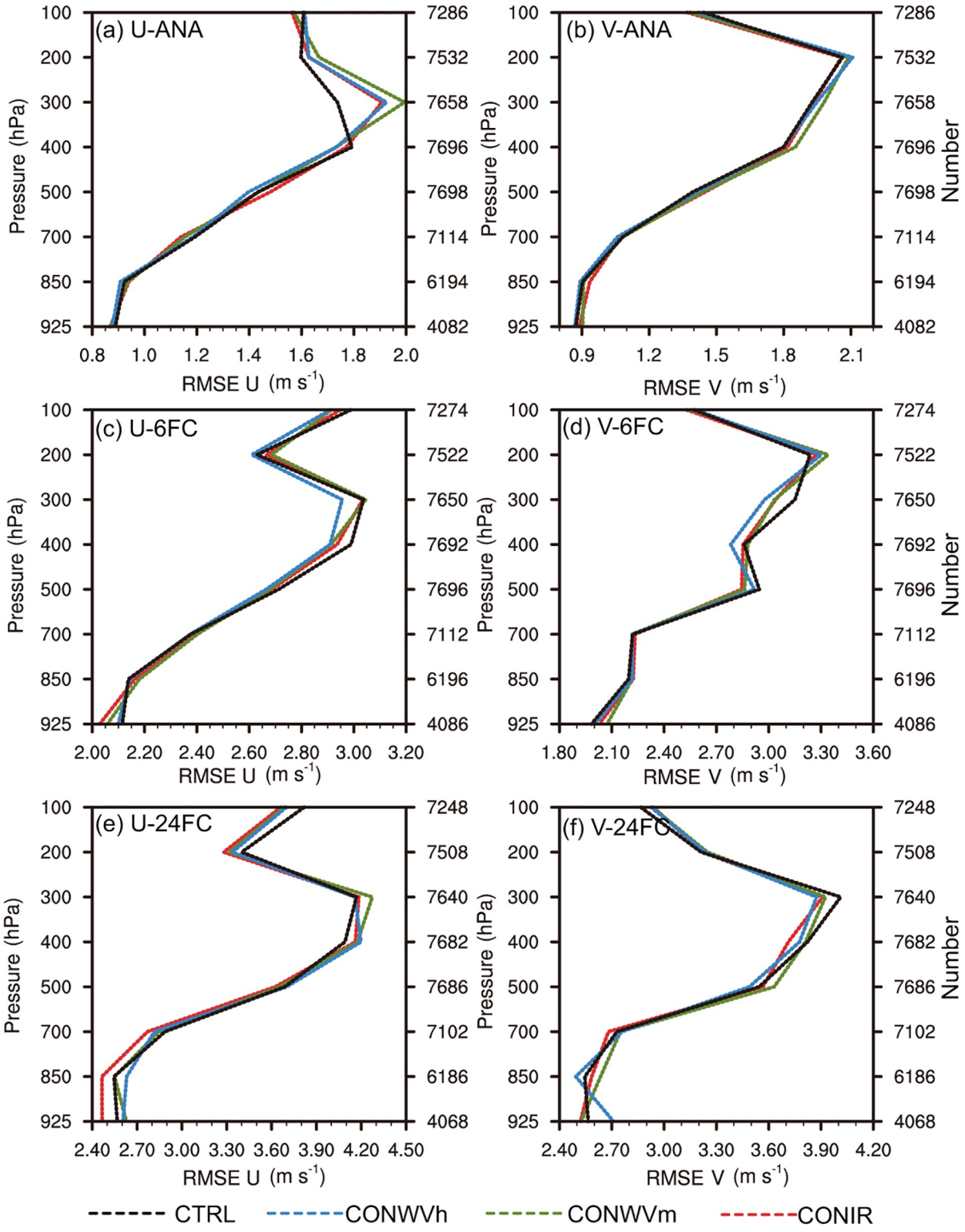

Fig. 9. Averaged vertical RMSE profiles for analyses and 6-h and 24-h forecasts in comparison with radiosonde data for CTRL and single-channel assimilation experiments.

from WV-High, while AMVs from IR can produce noticeable improvement in the lower layer after 12 h of forecasting.

5.2.2. *Precipitation forecast*

Several precipitation processes occur during the research period, so the impact of FY-4A AMVs on the precipitation forecasting skill is evaluated. The bias score (BS), threat score (TS), probability of detection (POD), and false alarm ratio (FAR) (formulae shown in Table 3) are used. The closer the BS, TS and POD are to 1, the higher the predic-

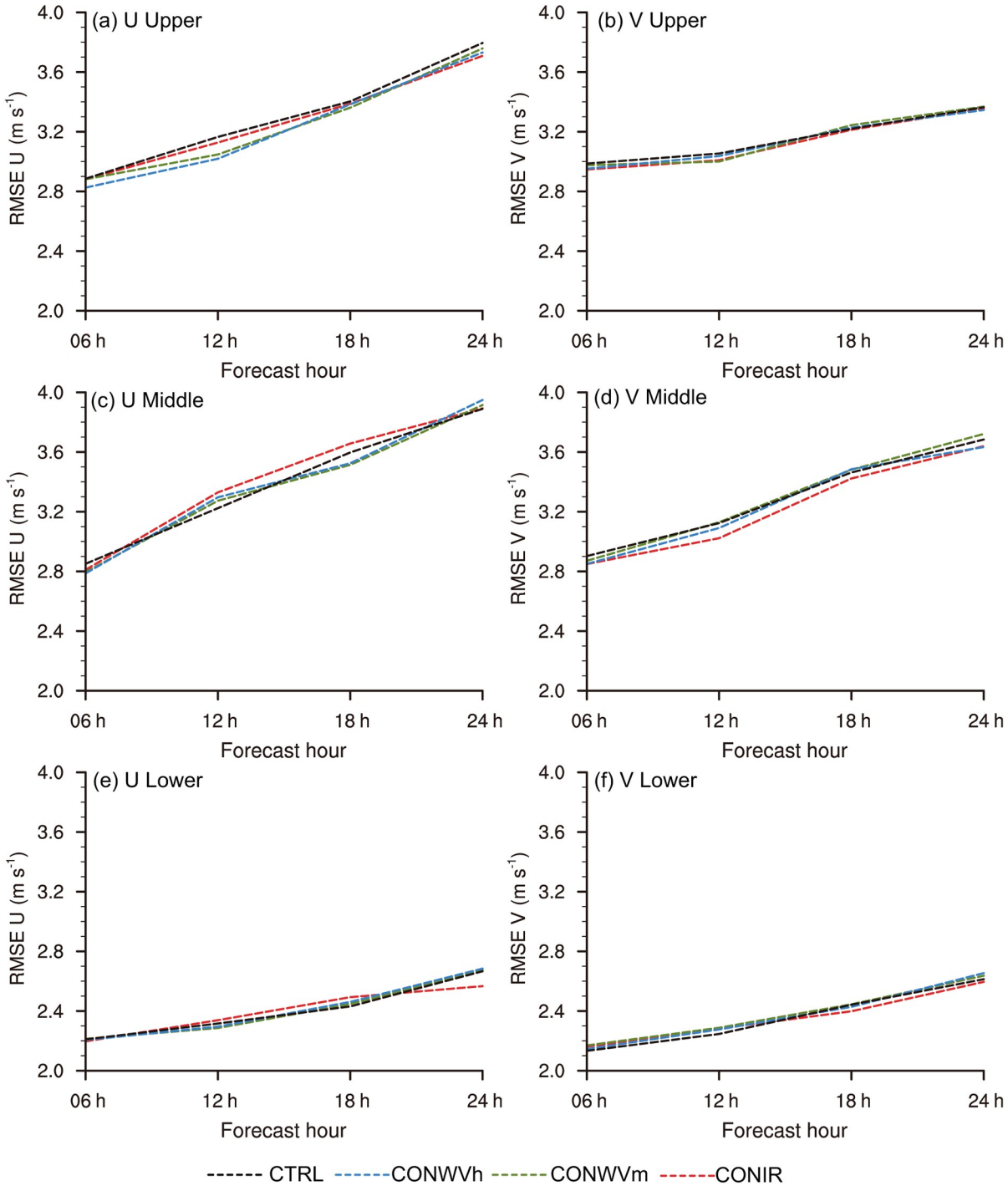

Fig. 10. Average RMSEs at different lead times for the (a, b) upper layer (above 400 hPa), (c, d) middle layer (400–700 hPa) and (e, f) lower layer (below 700 hPa) for the CTRL and single-channel assimilation experiments.

tion accuracy of precipitation; and the smaller the FAR, the fewer false alarms in the precipitation forecast. The precipitation data for comparison are the hourly observations from surface stations provided by the CMA.

The average TS, BS, POD and FAR for the 6-h accumulated precipitation with thresholds of 0.1 mm, 1.0 mm, 5.0 mm 10.0 mm and 25.0 mm are shown in Fig. 12. Compared to CTRL, the assimilation of the FY-4A AMVs results in a decrease in BS for 6-h accumulated precipitation with intensity between 1.0 mm and 10.0 mm, and CONIR has the smallest values. Besides, the average TS and POD in CONWVm and CONIR show a slight improvement in precipitation with thresholds between 1.0 mm and 10.0 mm. In addition, the FAR of the experiments assimilating FY-4A AMVs decrease when compared to CTRL, and CONIR produces the lowest FAR value. However, owing to the actual intensity of the 6-h accumulated precipitation from these rainfall events being lower than 25.0 mm, the added AMVs lead

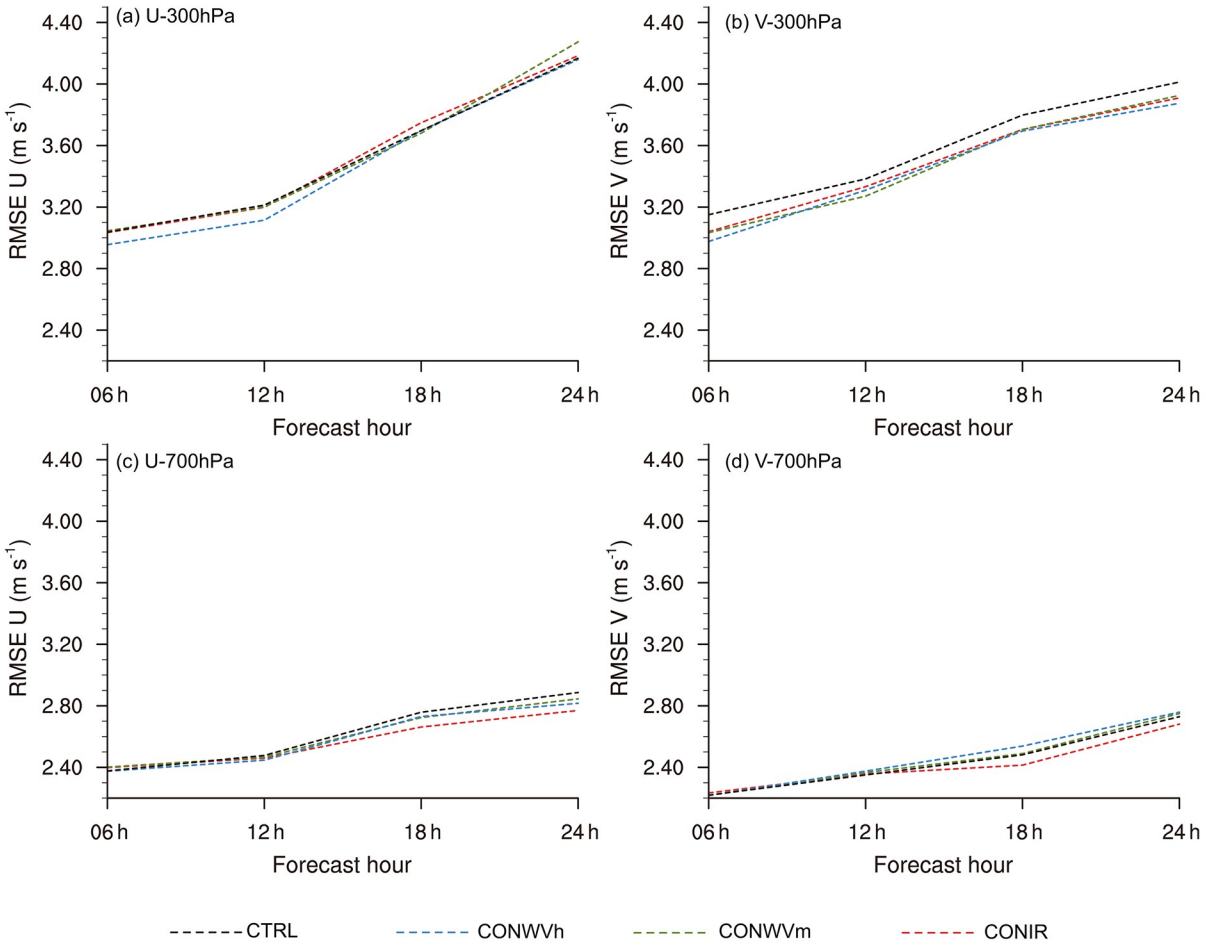

Fig. 11. RMSEs at 300 hPa and 700 hPa at different lead times for the CTRL and single-channel assimilation experiments.

Table 3. Four statistical indices for rainfall forecast skill.

Index	Formula
Bias Score (BS)	(hits + false alarms)/(hits + misses)
Threat Score (TS)	hits/(hits + false alarms + misses)
Probability of Detection (POD)	hits/(hits + misses)
False Alarm Ratio (FAR)	false alarms/(hits + false alarms)

to an under-prediction with the threshold of 25.0 mm, overall.

Generally, the results suggest that AMVs derived from the IR channel produce the largest improvement among the three channels. The reason may be that the precipitation intensity of these processes during the experiment is relatively weak and the vertical development relatively low. As a result, the wind of the lower layer in the IR channel has a positive impact on the precipitation.

5.3. *Verification for multi-channel assimilation*

Through the above discussion of the impact of assimilating single-channel AMVs on the analysis and forecasts, it can be concluded that the FY-4A AMVs from the water vapor channels mainly improve the wind field in the upper layer. Meanwhile, assimilating AMVs from IR has a slightly positive impact in the middle and lower layers. Next, to combine the advantages of the three channels, FY-4A AMVs from the three channels are simultaneously assimilated, and the impact on the forecast further analyzed.

Figure 13 displays the average RMSEs of the analysis and forecasts for the horizontal winds (U, V) of CTRL, CONALL and CONALL-DEF. Similar to Fig. 9, the assimilation of FY-4A AMVs derived from the three channels produces analyses a little inferior to that of CTRL, especially for the upper layer where a large number of AMVs are distributed, which is due to the rough spatial resolution of the radiosonde data. Also, the improvement from assimilating FY-4A AMVs will be seen after integrating for several hours. For example, the differences between the RMSEs of the experiments assimilating AMVs and that of CTRL decrease after six hours of model integration, and their RMSEs are relatively smaller than those of CTRL for the V component under 400 hPa. For the 24-h forecast, the RMSEs of U and

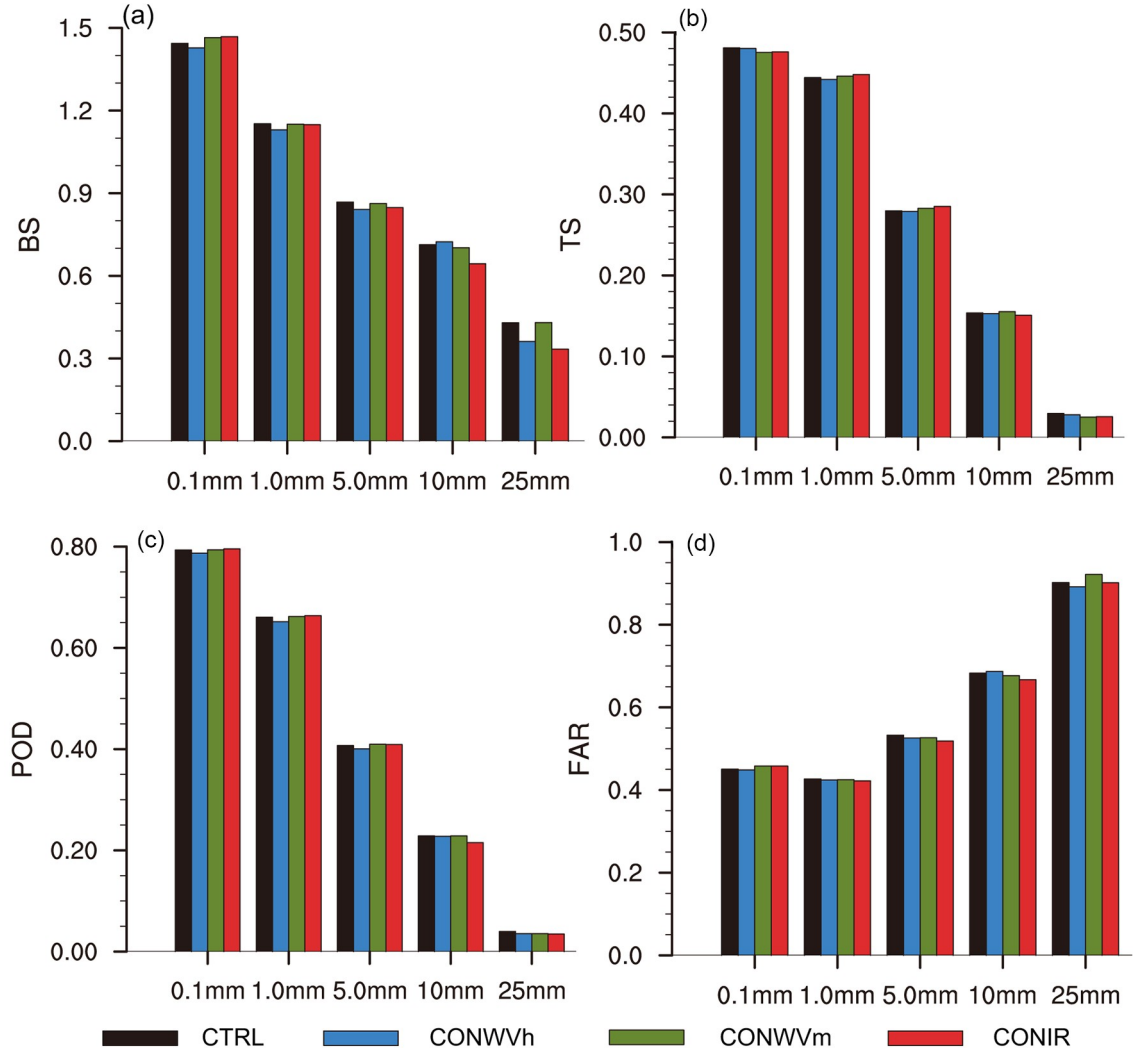

Fig. 12. Average BS (a), TS (b), POD (c) and FAR (d) for the 6-h accumulated precipitation with different thresholds for the CTRL and single-channel assimilation experiments.

V in CONALL and CONALL-DEF are smaller than those in CTRL at almost all levels. The main advantage of assimilating FY-4A AMVs in the *U* component gradually shifts from the upper layer to the middle and lower layer, while the improvement of the *V* component is still shown in the upper layer.

In addition, Fig. 13 also shows the impact of different observation errors on assimilation and prediction results. As can be seen from the RMSE profiles, when compared to CONALL-DEF (gray lines), assimilating FY-4A AMVs with new observation errors (purple lines) can clearly reduce the RMSEs of the horizontal wind components in almost all layers both in the analyses and 6-h and 24-h forecasts, which can serve as a reference for the significance of estimated observation error in new observation datasets.

Besides, according to the precipitation forecasting skill scores displayed in Fig. 14, except for the threshold of 0.1 mm, CONALL results in a decrease of BS and FAR when compared to CTRL. Moreover, the average TS and POD in CONALL show a slight improvement for precipitation with thresholds between 1.0 mm and 10.0 mm, which is similar to the result obtained in the single-channel assimilation.

6. Conclusions

In order to further promote the practical application of FY-4A satellite data in NWP, the features of FY-4A AMV products derived from the WV-High, WV-Mid and IR channels are analyzed in this paper and their observation errors estimated. Then, one-month single-channel and multi-channel data assimilation and forecasting experiments are carried out based on the operational RMAPS-ST system. The main results are as follows:

(1) FY-4A AMVs derived from the two water vapor channels are concentrated in the upper and middle layers, especially between 400 hPa and 200 hPa, while AMVs from IR have a maximum total number in the upper and lower layers. In addition, AMVs derived from the three channels show relatively normal PDF distributions of deviation from the reference field in the upper and middle layers, as do FY-

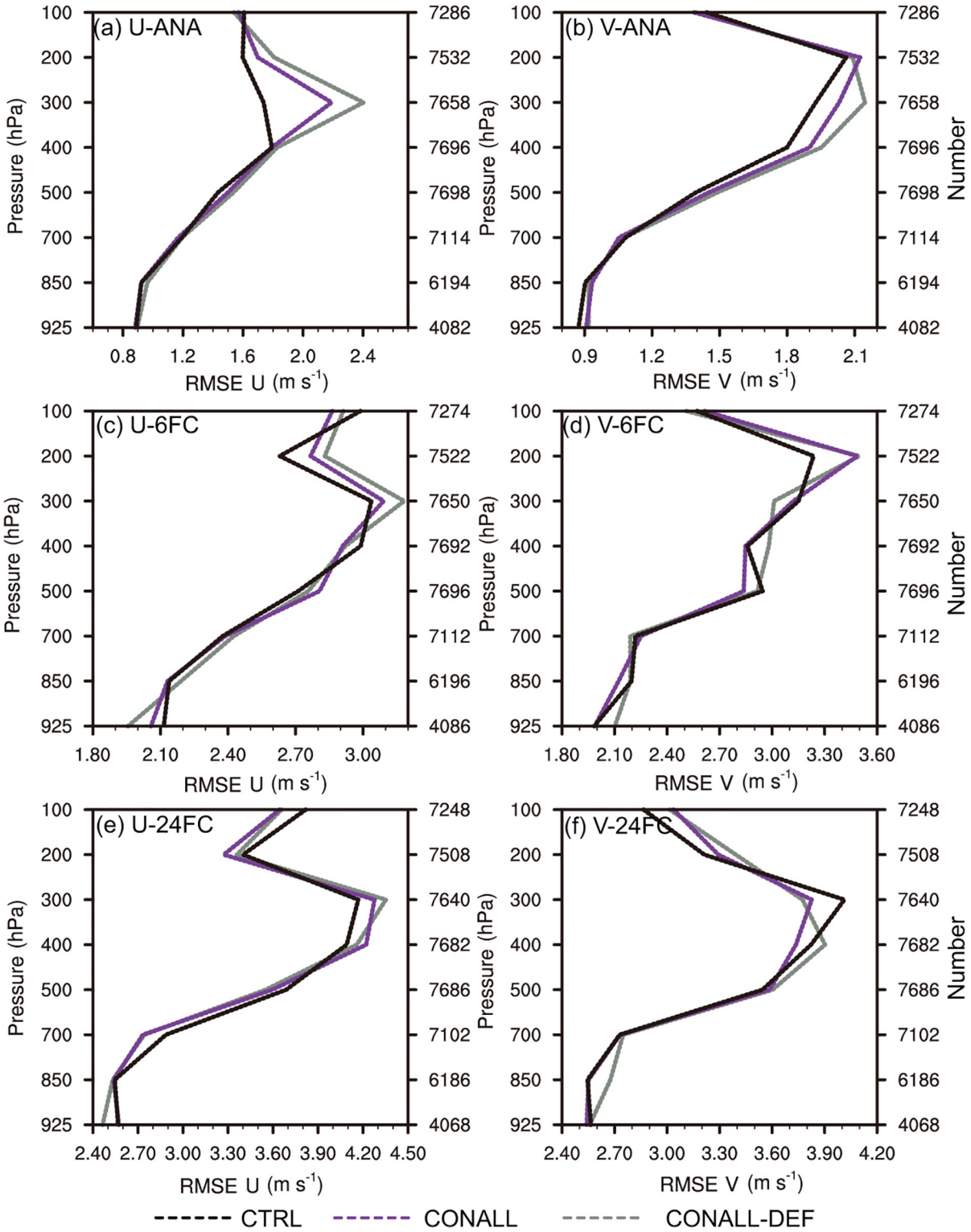

Fig. 13. Averaged vertical RMSE profiles for analyses and 6-h and 24-h forecasts in comparison with radiosonde data for CTRL, CONALL and CONALL-DEF.

4A AMVs in the lower layer derived from the IR channel.

(2) Observation errors of FY-4A AMV products have obvious vertical structures. The profiles of the three channels above 400 hPa are similar in structure and are quantitatively comparable. Between 400 hPa and 700 hPa, the observation errors of WV-High increase with height, while those of WV-Mid and IR decrease with height.

(3) The one-month single-channel data assimilation cycling and forecasting experiments demonstrate that assimilating FY-4A AMVs improves wind forecasts. Moreover,

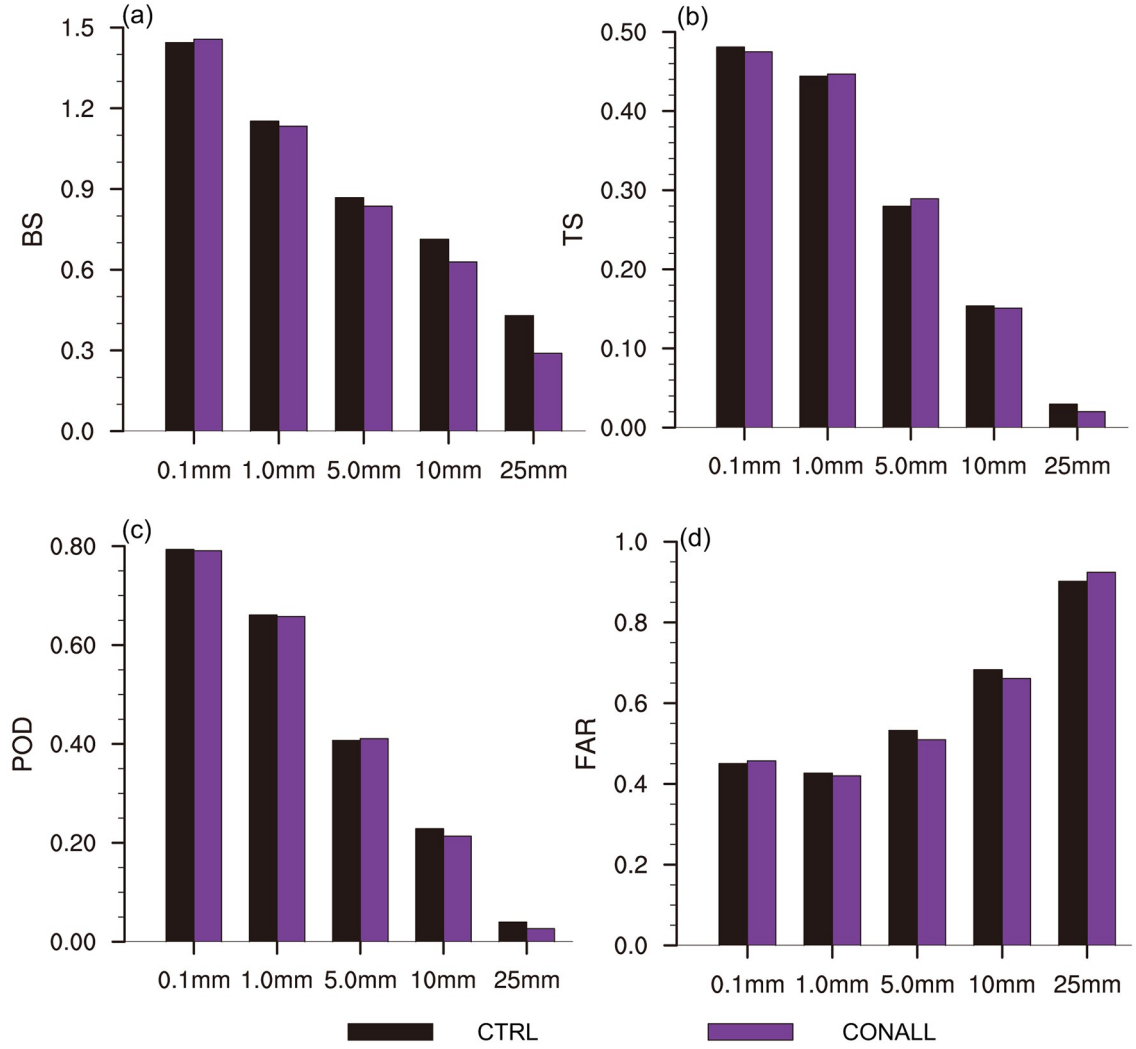

Fig. 14. Average BS (a), TS (b), POD (c) and FAR (d) for the 6-h accumulated precipitation with different thresholds for CTRL and CONALL.

AMVs from WV-High produce more apparent improvement in the wind field in the upper layer, and AMVs from IR can achieve more obvious positive effects in the lower layer. Furthermore, assimilating AMVs from IR produces higher skill scores for medium and moderate precipitation than the other channels owing to its good quality of data in the lower layer.

(4) Simultaneous assimilation of FY-4A AMVs from the three channels combines the advantages of assimilating the three individual channels to improve the forecasts in the upper, middle and lower layers at the same time. Moreover, simultaneous assimilation has an obvious positive impact on the precipitation forecast with thresholds between 1.0 mm and 10.0 mm.

Considering that the AMV products derived from the FY-4A satellite are still being studied, more comprehensive and detailed comparisons and evaluations should be conducted in the future by combining the AMV products derived from other satellites, such as those from Himawari-8. In addition, stricter quality-control procedures for FY-4A AMVs should be implemented to reduce the correlation between AMVs. Moreover, the experimental scheme of simultaneous assimilation of FY-4A AMVs of the three channels still needs to be improved, and duplication of the AMVs between different channels for assimilation should be further considered.

Acknowledgements. This research was funded by the National Key Research and Development Plan (Grant No. 2018YFC1507105). We wish to thank Dr. Xiaohu ZHANG from the National Satellite Meteorological Center of China for providing the AMV data and other relevant help. We also thank the Editor and reviewers for their comments and suggestions for improving the manuscript.

REFERENCES

Bedka, K. M., C. S. Velden, R. A. Petersen, W. F. Feltz, and J. R. Mecikalski, 2008: Comparisons of satellite-derived atmospheric motion vectors, rawinsondes, and NOAA wind profiler observations. *J. Appl. Meteorol. Climatol.*, **48**,

1542–1561, https://doi.org/10.1175/2009jamc1867.1.

Benjamin, S. G., B. E. Schwartz, and R. E. Cole, 1998: Accuracy of ACARS wind and temperature observations determined by collocation. *Wea. Forecasting*, **14**, 1032–1038, https://doi.org/10.1175/1520-0434(1999)014<1032:AOAWAT>2.0.CO;2.

Berger, H., R. Langland, C. S. Velden, C. A. Reynolds, and P. M. Pauley, 2011: Impact of enhanced satellite-derived atmospheric motion vector observations on numerical tropical cyclone track forecasts in the Western North Pacific during TPARC/TCS-08. *J. Appl. Meteorol. Climatol.*, **50**, 2309–2318, https://doi.org/10.1175/jamc-d-11-019.1.

Bormann, N., S. Saarinen, G. Kelly, and J.-N. Thépaut, 2003: The spatial structure of observation errors in atmospheric motion vectors from geostationary satellite data. *Mon. Wea. Rev.*, **131**, 706–718, https://doi.org/10.1175/1520-0493(2003)131<0706:TSSOOE>2.0.CO;2.

Chen, M., M. X. Chen, and S. Y. Fan, 2014: The real-time radar radial velocity 3DVar assimilation experiments for application to an operational forecast model in North China. *Acta Meteorological Sinica*, **72**, 658–677, https://doi.org/10.11676/qxxb2014.070. (in Chinese with English abstract)

Cordoba, M., S. L. Dance, G. A. Kelly, N. K. Nichols, and J. A. Waller, 2017: Diagnosing atmospheric motion vector observation errors for an operational high-resolution data assimilation system. *Quart. J. Roy. Meteor. Soc.*, **143**, 333–341, https://doi.org/10.1002/qj.2925.

Deb, S. K., C. M. Kishtawal, I. Kaur, P. K. Pal, and A. S. Kiran Kumar, 2015: Assessment of a new quality control technique in the retrieval of atmospheric motion vectors. *Meteorological Applications*, **22**, 178–186, https://doi.org/10.1002/met.1433.

Deb, S. K., P. Kumar, P. K. Pal, and P. C. Joshi, 2011: Assimilation of INSAT data in the simulation of the recent tropical Cyclone Aila. *Int. J. Remote Sens.*, **32**, 5135–5155, https://doi.org/10.1080/01431161.2010.494640.

Desroziers, G., L. Berre, B. Chapnik, and P. Poli, 2005: Diagnosis of observation, background and analysis-error statistics in observation space. *Quart. J. Roy. Meteor. Soc.*, **131**, 3385–3396, https://doi.org/10.1256/qj.05.108.

Dong, Y.-H., 2016: FY-4 meteorological satellite and its application prospect. *Aerospace Shanghai*, **33**, 1–8, https://doi.org/10.19328/j.cnki.1006-1630.2016.02.001. (in Chinese with English abstract)

Errico, R. M., D. J. Stensrud, and K. D. Raeder, 2001: Estimation of the error distributions of precipitation produced by convective parametrization schemes. *Quart. J. Roy. Meteor. Soc.*, **127**, 2495–2512, https://doi.org/10.1002/qj.49712757802.

Fan, S. Y., H. L. Wang, M. Chen, and H. Gao, 2013: Study of the data assimilation of radar reflectivity with the WRF 3D-Var. *Acta Meteorological Sinica*, **71**, 527–537, https://doi.org/10.11676/qxxb2013.032. (in Chinese with English abstract)

Feng, W., Q. L. Wan, Z. T. Chen, W. Y. Ding, and Y. Y. Huang, 2008: Hourly assimilation of cloud motion winds and its impact on torrential rain forecast. *Acta Meteorological Sinica*, **66**, 500–512, https://doi.org/10.3321/j.issn:0577-6619.2008.04.003. (in Chinese with English abstract)

Gao, F., X. Y. Zhang, N. A. Jacobs, X.-Y. Huang, X. Zhang, and P. P. Childs, 2012: Estimation of TAMDAR observational error and assimilation experiments. *Wea. Forecasting*, **27**, 856–877, https://doi.org/10.1175/WAF-D-11-00120.1.

Goerss, J. S., 2009: Impact of satellite observations on the tropical cyclone track forecasts of the navy operational global atmospheric prediction system. *Mon. Wea. Rev.*, **137**, 41–50, https://doi.org/10.1175/2008mwr2601.1.

He, J., M. Chen, J. Q. Zhong, and X. Y. Hong, 2019: A study of three-dimensional radar reflectivity mosaic assimilation in the regional forecasting model for North China. *Acta Meteorological Sinica*, **77**, 210–232, https://doi.org/10.11676/qxxb2019.005. (in Chinese with English abstract)

Hollingsworth, A., and P. Lönnberg, 1986: The statistical structure of short-range forecast errors as determined from radiosonde data. Part I: The wind field. *Tellus A: Dynamic Meteorology and Oceanography*, **38**, 111–136, https://doi.org/10.1111/j.1600-0870.1986.tb00460.x.

Holmlund, K., 1998: The utilization of statistical properties of satellite-derived atmospheric motion vectors to derive quality indicators. *Wea. Forecasting*, **13**, 1093–1104, https://doi.org/10.1175/1520-0434(1998)013<1093:TUOSPO>2.0.CO;2.

Honda, T., S. Kotsuki, G.-Y. Lien, Y. Maejima, K. Okamoto, and T. Miyoshi, 2018: Assimilation of Himawari-8 all-sky radiance every 10 minutes: Impact on precipitation and flood risk prediction. *J. Geophys. Res.*, **123**, 965–976, https://doi.org/10.1002/2017JD027096.

Hsiao, L.-F., D.-S. Chen, Y.-H. Kuo, Y.-R. Guo, T.-C. Yeh, J.-S. Hong, C.-T. Fong, and C.-S. Lee, 2012: Application of WRF 3DVAR to operational typhoon prediction in Taiwan: Impact of outer loop and partial cycling approaches. *Wea. Forecasting*, **27**, 1249–1263, https://doi.org/10.1175/WAF-D-11-00131.1.

Iacono, M. J., J. S. Delamere, E. J. Mlawer, M. W. Shephard, S. A. Clough, and W. D. Collins, 2008: Radiative forcing by long-lived greenhouse gases: Calculations with the AER radiative transfer models. *J. Geophys. Res.*, **113**(D13), D13103, https://doi.org/10.1029/2008JD009944.

Joo, S., J. Eyre, and R. Marriott, 2013: The impact of METOP and other satellite data within the Met Office global NWP system using an adjoint-based sensitivity method. *Mon. Wea. Rev.*, **141**, 3331–3342, https://doi.org/10.1175/MWR-D-12-00232.1.

Kain, J. S., 2004: The Kain-Fritsch convective parameterization: An update. *J. Appl. Meteorol.*, **43**, 170–181, https://doi.org/10.1175/1520-0450(2004)043<0170:tkcpau>2.0.co;2.

Kaur, I., P. Kumar, S. K. Deb, C. M. Kishtawal, P. K. Pal, and R. Kumar, 2015: Impact of Kalpana-1 retrieved atmospheric motion vectors on mesoscale model forecast during summer monsoon 2011. *Theor. Appl. Climatol.*, **120**, 587–599, https://doi.org/10.1007/s00704-014-1197-9.

Kim, D.-H., and H. M. Kim, 2018: Effect of assimilating *Himawari-8* atmospheric motion vectors on forecast errors over East Asia. *J. Atmos. Oceanic Technol.*, **35**, 1737–1752, https://doi.org/10.1175/JTECH-D-17-0093.1.

Kirby, S. F., 2004: Model evaluation tool. ARL-TR-3373, White Sands Missile Range, NM, 1–23.

Kunii, M., M. Otsuka, K. Shimoji, and H. Seko, 2016: Ensemble data assimilation and forecast experiments for the September 2015 heavy rainfall event in Kanto and Tohoku Regions with atmospheric motion vectors from Himawari-8. *SOLA*, **12**, 209–214, https://doi.org/10.2151/sola.2016-042.

Li, J. L., J. Li, C. Velden, P. Wang, T. J. Schmit, and J. Sippel, 2020: Impact of rapid-scan-based dynamical information from GOES-16 on HWRF hurricane forecasts. *J. Geophys. Res.*, **125**, e2019JD031647, https://doi.org/10.1029/2019

JD031647.

Lu, F., and Coauthors, 2017: FY-4 geostationary meteorological satellite imaging characteristics and its application prospects. *Journal of Marine Meteorology*, **37**, 1–12, https://doi.org/10.19513/j.cnki.issn2096-3599.2017.02.001. (in Chinese with English abstract)

Menzel, W. P., 2001: Cloud tracking with satellite imagery: From the pioneering work of Ted Fujita to the present. *Bull. Amer. Meteor. Soc.*, **82**, 33–48, https://doi.org/10.1175/1520-0477(2001)082<0033:CTWSIF>2.3.CO;2.

Nieman, S. J., J. Schmetz, and W. P. Menzel, 1993: A comparison of several techniques to assign heights to cloud tracers. *J. Appl. Meteorol.*, **50**, 1559–1568, https://doi.org/10.1175/1520-0450(1993)032<1559:ACOSTT>2.0.CO;2.

Otsuka, M., H. Seko, K. Shimoji, and K. Yamashita, 2018: Characteristics of Himawari-8 rapid scan atmospheric motion vectors utilized in mesoscale data assimilation. *J. Meteor. Soc. Japan*, **96B**, 111–131, https://doi.org/10.2151/jmsj.2018-034.

Otsuka, M., M. Kunii, H. Seko, K. Shimoji, M. Hayashi, and K. Yamashita, 2015: Assimilation experiments of MTSAT rapid scan atmospheric motion vectors on a heavy rainfall event. *J. Meteor. Soc. Japan*, **93**, 459–475, https://doi.org/10.2151/jmsj.2015-030.

Ren, S. L., J. Y. Jiang, and J. M. Xu, 2014: Application of upper troposphere circulation revealed by the satellite IR3 channel to heavy rainfall events analysis in the east side of South Asia High. *Meteorological Monthly*, **40**, 697–705, https://doi.org/10.7519/j.issn.1000-0526.2014.06.006. (in Chinese with English abstract)

Schmetz, J., K. Holmlund, J. Hoffman, B. Strauss, B. Mason, V. Gaertner, A. Koch, and L. Berg, 1993: Operational cloud-motion winds from meteosat infrared images. *J. Appl. Meteorol.*, **32**, 1206–1225, https://doi.org/10.1175/1520-0450(1993)032<1206:OCMWFM>2.0.CO;2.

Soden, J. B., C. S. Velden, and R. E. Tuleya, 2001: The impact of satellite winds on experimental GFDL hurricane model forecasts. *Mon. Wea. Rev.*, **129**, 835–852, https://doi.org/10.1175/1520-0493(2001)129<0835:TIOSWO>2.0.CO;2.

Thompson, G., P. R. Field, R. M. Rasmussen, and W. D. Hall, 2008: Explicit forecasts of winter precipitation using an improved bulk microphysics scheme. Part Ⅱ: Implementation of a new snow parameterization. *Mon. Wea. Rev.*, **136**, 5095–5115, https://doi.org/10.1175/2008MWR2387.1.

Velden, C. S., T. L. Olander, and S. Wanzong, 1998: The impact of multispectral *GOES-8* wind information on Atlantic tropical cyclone track forecasts in 1995. Part I: Dataset methodology, description, and case analysis. *Mon. Wea. Rev.*, **126**, 1202–1218, https://doi.org/10.1175/1520-0493(1998)126<1202:TIOMGW>2.0.CO;2.

Velden, C. S., C. M. Hayden, S. J. W. Nieman, W. P. Menzel, S. Wanzong, and J. S. Goerss, 1997: Upper-tropospheric winds derived from geostationary satellite water vapor observations. *Bull. Amer. Meteor. Soc.*, **78**, 173–196, https://doi.org/10.1175/1520-0477(1997)078<0173:UTWDFG>2.0.CO;2.

Velden, C., W. E. Lewis, W. Bresky, D. Stettner, J. Daniels, and S. Wanzong, 2017: Assimilation of high-resolution satellite-derived atmospheric motion vectors: Impact on HWRF forecasts of tropical cyclone track and intensity. *Mon. Wea. Rev.*, **145**, 1107–1125, https://doi.org/10.1175/MWR-D-16-0229.1.

Wan, X. M., W. Han, W. H. Tian, and X. H. He, 2018: The application of intensive FY-2G AMVs in GRAPES_RAFS. *Plateau Meteorology*, **37**, 1083–1093, https://doi.org/10.7522/j.issn.1000-0534.2017.00089. (in Chinese with English abstract)

Wan, X. M., J. D. Gong, W. Han, and W. H. Tian, 2019: The evaluation of FY-4A AMVs in GRAPES_RAFS. *Meteorological Monthly*, **45**, 458–468, https://doi.org/10.7519/j.issn.1000-0526.2019.04.002. (in Chinese with English abstract)

Wang, D. L., X. D. Liang, Y. H. Duan, and J. C. L. Chan, 2006: Impact of four-dimensional variational data assimilation of atmospheric motion vectors on tropical cyclone track forecasts. *Wea. Forecasting*, **21**, 663–669, https://doi.org/10.1175/waf940.1.

Wang, G. Q., and X. Shen, 2018: The FY-4 radiometer imager and the application of its data in the satellite meteorology. *Chinese Journal of Nature*, **40**, 1–11, https://doi.org/10.3969/j.issn.0253-9608.2018.01.001.(inChinesewithEnglishabstract). (in Chinese with English abstract)

Wu, T.-C., H. Liu, S. J. Majumdar, C. S. Velden, and J. L. Anderson, 2014: Influence of assimilating satellite-derived atmospheric motion vector observations on numerical analyses and forecasts of tropical cyclone track and intensity. *Mon. Wea. Rev.*, **142**, 49–71, https://doi.org/10.1175/mwr-d-13-00023.1.

Xie, Y. H., S. Y. Fan, M. Chen, J. C. Shi, J. Q. Zhong, and X. Y. Zhang, 2019: An assessment of satellite radiance data assimilation in RMAPS. *Remote Sensing*, **11**, 54, https://doi.org/10.3390/rs11010054.

Yamashita, K., 2012: An observing system experiment of MTSAT rapid scan AMV using JMA meso-scale operational NWP system. *Proc. 11th International Winds Workshop*, Auckland, New Zealand, S4–15.

Yang, L., Z. H. Wang, Y. L. Chu, H. Zhao, and M. Tang, 2014: Water vapor motion signal extraction from FY-2E longwave infrared window images for cloud-free regions: The temporal difference technique. *Adv. Atmos. Sci.*, **31**, 1386–1394, https://doi.org/10.1007/s00376-014-3165-9.

Zhang, Z. Q., and Coauthors, 2017: Application and development of FY-4 meteorological satellite. *Aerospace Shanghai*, **34**, 8–19, https://doi.org/10.19328/j.cnki.1006-1630.2017.04.002. (in Chinese with English abstract)

Zhao, L., J. Shang, X. H. Feng, and Z. Q. Zhang, 2019: Typical observation area design of FY-4 geostationary meteorological satellite Imager. *Advances in Meteorological Science and Technology*, **9**, 37–40, https://doi.org/10.3969/j.issn.2095-1973.2019.01.006. (in Chinese with English abstract)